ELSEVIER

Journal of Nuclear Materials 300 (2002) 161–177

journal of nuclear materials

www.elsevier.com/locate/jnucmat

Mechanical and thermomechanical properties of commercially pure chromium and chromium alloys

Uwe Holzwarth *, Hermann Stamm

European Commission, Joint Research Centre, Via E. Fermi 1 (T.P.500), I-21020 Ispra (VA), Italy

Received 11 July 2001; accepted 9 November 2001

Abstract

The mechanical and thermal properties of commercially pure chromium and the chromium-based alloys Cr–5Fe–$1Y_2O_3$ and Cr–44Fe–5Al–0.3Ti–$0.5Y_2O_3$ have been investigated in order to determine the thermal stress factor of these materials and to assess their capability to withstand high-thermal loads in fusion applications. Especially the alloy Cr–5Fe–$1Y_2O_3$ combines sufficient mechanical strength at temperatures up to 1000 °C, high-thermal conductivity and a low-thermal expansion coefficient to yield the lowest thermal stress factor of all metallic candidate materials for first wall and blanket applications. The high-ductile-to-brittle transition temperature may lead to a rather high value for the lower operation-temperature limit.

1. Introduction

Chromium and chromium alloys have been studied since the fifties in order to explore possible high-temperature application in jet engines [1,2]. These materials exhibit a favourable strength-to-density ratio combined with a high melting point (pure chromium: 1863 °C [3]) and an excellent corrosion resistance [4]. However, embrittlement from nitrogen contamination at elevated temperatures, the high ductile-to-brittle transition temperature (DBTT) and resulting problems of low toughness and ductility with their impact on shaping, welding and manufacture routes [1] limited the interest in chromium-based alloys. Industrial applications of pure chromium were confined to functional coatings in electronics and optics, to coatings for improving corrosion and wear resistance and brilliant coatings for decoration purposes [5]. Recent applications of chromium-based alloys as structural material in fuel cells rely on the excellent corrosion behaviour under the specific environmental and thermal conditions, the electrical conductivity of the oxide layer and the high strength at elevated service temperatures [6]. Moreover, up to 1000 °C the thermal expansion coefficients of the alloys Cr–5Fe–$1Y_2O_3$ and Cr–$0.4La_2O_3$ excellently match that of ZrO_2 used as solid electrolyte [7]. At temperatures above 1400 °C the protective Cr_2O_3 surface layer becomes instable. This motivated the development of the alloy Cr–44Fe–5Al–0.3Ti–$0.5Y_2O_3$ that is better protected by a more resistant Al_2O_3 layer. Moreover, the stability of the oxide layer additionally reduces the susceptibility of the material to stress corrosion cracking [8].

Chromium and chromium alloys regained attraction as potential structural material in fusion reactors due to their excellent low-activation characteristics [9–11] and their potential high service temperature of up to 1000 °C [12]. Calculations by Zucchetti and Merola [9] simulating the neutron activation of the alloys Cr–5Fe–$1Y_2O_3$ and Cr–44Fe–5Al–0.3Ti–$0.5Y_2O_3$ under service conditions showed that a first wall component made of Cr–5Fe–$1Y_2O_3$ may be classified as *low-level waste* (dose rate $\leqslant$ 2 mSv/h [13]) after 50 years of cooling [9]. Though more recently Dyomina et al. [14] published that SiC/SiC fibre-matrix composites and high-purity V–4Cr–4Ti alloy may nearly reach the low-activation properties of

* Corresponding author. Tel.: +39-0332 785 194; fax: +39-0332 789 385.

E-mail address: uwe.holzwarth@jrc.it (U. Holzwarth).

0022-3115/02/$ - see front matter
PII: S0022-3115(01)00745-0

Cr–5Fe–1Y_2O_3, chromium alloys may further be improved by reducing molybdenum impurities. This would allow even hands-on recycling after 100 years of cooling [9].

Fusion reactor materials have to withstand the irradiation with a high flux of 14 MeV fusion neutrons, protons and alpha particles leading to gas bubble formation, swelling or void formation with possible problems of dimensional stability, phase stability, and the degradation of mechanical and thermal properties [15–19]. According to the design study of the International Thermonuclear Experimental Reactor (ITER), the blanket structure is cooled by water [20] which limits the operation temperature of the structural material to about 300 °C. However, in next generation machines like the demonstration reactor DEMO the structural material is supposed to operate at temperatures between 500 and 700 °C [21]. For the breeding blanket temperatures up to 950 °C are desired [19].

First wall and blanket components are subjected to cyclic thermal loading. The temperature gradient ΔT caused by an energy flux $\dot{q}$ per unit area in a wall of thickness d is given by

$$\Delta T = \frac{\dot{q}d}{\lambda}, \tag{1}$$

where λ denotes the thermal conductivity of the wall or blanket material. Inserting this expression in the formula for the thermal stress, which is proportional to ΔT, results in

$$\sigma_{\text{thermal}} = \frac{\alpha E\ \Delta T}{(1-\nu)} = \frac{\alpha E d\dot{q}}{\lambda(1-\nu)}, \tag{2}$$

where E and ν denote the Young's modulus and the Poisson coefficient, respectively. α stands for the thermal expansion coefficient of the material. With $\dot{q}$ given by the service conditions and d depending on the construction, all material properties in Eq. (2) can be summarized by the so-called thermal stress factor. The thermal stress factor Θ or the stress factor Θ^* normalized to the yield stress σ_y defined as

$$\Theta = \frac{\alpha E}{\lambda(1-\nu)} \quad \text{and} \quad \Theta^* = \frac{\alpha E}{\sigma_y \lambda(1-\nu)} \tag{3}$$

give an estimate of the magnitude of thermal stresses in materials exposed to thermal transients.

The maximum allowable temperature may also be limited by the strength of the material, its creep properties and the chemical compatibility with the coolant leading to potential corrosion problems. Depending on the reactor design liquid lithium or water will be used as coolant. Further limits for the maximum allowable temperature may be set by the pickup of interstitial solutes especially in hydrogen and oxygen environments. The minimum service temperature is essentially determined by the DBTT and by irradiation hardening shifting up the DBTT. Additionally, attention has to be paid to helium embrittlement and gas bubble formation.

So far chromium and chromium-based alloys did not attract as much attention as their competitors as potential structural materials like reduced activation austenitic steels, reduced activation ferritic martensitic steels [22–26], vanadium alloys [15,27–29] and SiC/SiC ceramic fibre-matrix composites [30–32]. In spite of problems with phase stability and irradiation induced segregation [33], activities are still focused on reduced activation steels, having the advantage of well established and mastered technologies for production, shaping and joining. Consequently current efforts aim at increasing high-temperature strength of steels by dispersion hardening [34]. The development risk of vanadium and chromium alloys and SiC/SiC is considered as high because production routes, shaping and joining processes are still to be developed and problems caused by the inherent brittleness of chromium alloys and ceramic fibre-matrix composites are still to overcome [17]. Among these materials chromium alloys and SiC/SiC fibre-matrix composites promise service temperatures up to 1000 °C, whereas the application of vanadium alloys will be limited in the range between 430 and 750 °C [22,28].

The development of chromium alloys for fuel cell applications resulted in powder metallurgical processing routes which allow the production and shaping of large batches of material with control of interstitial and substitutional impurities. Although chromium alloys are still expensive, a reduction in price by a factor of 10 can be expected if a large scale industrial production can be established [7]. The commercial availability of pure chromium and oxide particle strengthened chromium alloys, their low-activation property and the potential to withstand severe cyclic thermal loading motivated studies on their possible application in fusion reactors, carried out at the Joint Research Centre (JRC) of the European Commission at Ispra, Italy. The investigations aimed at a complete characterization of the mechanical and thermomechanical properties of the alloys and on a possible improvement of their ductility by microstructure refinement. Since fusion materials activities at the JRC were discontinued, planned examinations of irradiation effects were not carried out.

2. Materials and material processing

The examined materials were the commercially available pure chromium Ducropur™ (trademark of Metallwerke Plansee AG, Austria) and the alloys Cr–5Fe–1Y_2O_3 and Cr–44Fe–5Al–0.3Ti–0.5Y_2O_3 produced

Table 1
Chemical composition of the commercially available pure chromium (short name: Ducropur™) and the alloys Cr–5Fe–1Y_2O_3 (short name: Cr–5Fe) and Cr–44Fe–5Al–0.3Ti–0.5Y_2O_3 (short name: Cr–44Fe) [9]

Elements	Ducropur	Cr–5Fe	Cr–44Fe	State
Cr	99.7 wt%	Balance	Balance	Components
Fe	<0.25 wt%	5.3 wt%	43.6 wt%	
Y	–	0.68 wt%	0.37 wt%	
Al	<0.001 wt%	<0.001 wt%	4.77 wt%	
Ti	–	–	0.21 wt%	
O	<0.01 wt%	0.43 wt%	0.31 wt%	
N	<50 wt.ppm	115 wt.ppm	270 wt.ppm	Impurities
H	5 wt.ppm	5 wt.ppm	5 wt.ppm	
C	<100 wt.ppm	15 wt.ppm	98 wt.ppm	
Ca	20 wt.ppm	20 wt.ppm	20 wt.ppm	
Cu	25 wt.ppm	25 wt.ppm	25 wt.ppm	
K	5 wt.ppm	5 wt.ppm	5 wt.ppm	
Mg	5 wt.ppm	5 wt.ppm	5 wt.ppm	
Mo	100 wt.ppm	100 wt.ppm	100 wt.ppm	
Na	10 wt.ppm	10 wt.ppm	10 wt.ppm	
Ni	20 wt.ppm	20 wt.ppm	20 wt.ppm	
P	10 wt.ppm	10 wt.ppm	10 wt.ppm	
Pb	5 wt.ppm	5 wt.ppm	5 wt.ppm	
S	10 wt.ppm	10 wt.ppm	10 wt.ppm	
Si	60 wt.ppm	60 wt.ppm	60 wt.ppm	
W	100 wt.ppm	100 wt.ppm	100 wt.ppm	

by the Metallwerke Plansee AG, Austria. Their composition is reported in Table 1.

The material was available in form of plates of the dimensions 350 mm × 305 mm and a thickness of up to 15 mm. The production process is outlined in the product presentation sheet by Plansee AG [7] and more detailed in the doctoral thesis of Janousek [5]. Exact process parameters are confidential know-how of Plansee AG.

The base material was electrolytically deposited and degassed pure chromium powder. For a survey on the production of chromium powders the reader is referred to Sully and Brandes [35]. Iron was added as elementary iron powder, titanium in form of titanium hydride, and Y_2O_3 for oxide particle dispersion hardening as powder [5]. The particle size of the powders of the base materials was between 50 and 250 μm. In spite of mechanical alloying under a reducing hydrogen atmosphere the reduction of the particle size to about 10 μm was accompanied by an increase of the oxygen and nitrogen contents by a factor of two and five, respectively [5]. The mechanically alloyed powder was cold pressed thereby achieving about 60% of the theoretical density. A first sintering step was performed at about 1500 °C in a hydrogen atmosphere in order to reduce interstitial impurities. The material was then vacuum sealed in a steel capsule and hot rolled in a series of steps in order to obtain the full density of the material and the desired dimensions. Between the various rolling steps the material was annealed in order to reduce internal stresses and to improve its ductility [5]. After rolling, the steel capsules were removed in an acid bath. The interdiffusion layer was removed by grinding [5].

Various rolling steps with intermediate thermal treatments may be replaced in future by a single hot isostatic pressing process. This is simpler, faster and produces an isotropic structure with low-internal stresses, in contrast to the textured microstructure after rolling [5].

Microstructural investigations on the materials purchased from Plansee were performed by optical and scanning electron microscopy (SEM). A grain size of 82 μm in Ducropur, 11 μm in Cr–5Fe–1Y_2O_3 and 200 μm in Cr–44Fe–5Al–0.3Ti–0.5Y_2O_3 was determined after electrolytical etching using 20 ml nitric acid and 60 ml hydrochloric acid as well as the linear intercept method according to the standard ASTM E112-88 [36]. Fig. 1 shows optical micrographs of the different microstructure of the materials under investigation.

Cr–5Fe–1Y_2O_3 has extensively been studied by Janousek [5]. Transmission electron microscopy revealed a bimodal distribution of coarse and fine particles of 0.56 and 0.02 μm in size and a mean interparticle distance of 5.2 and 0.06 μm, respectively. Although the fine dispersoids were only present in about 40% of the bulk volume, the brittleness of pure chromium so far impeded

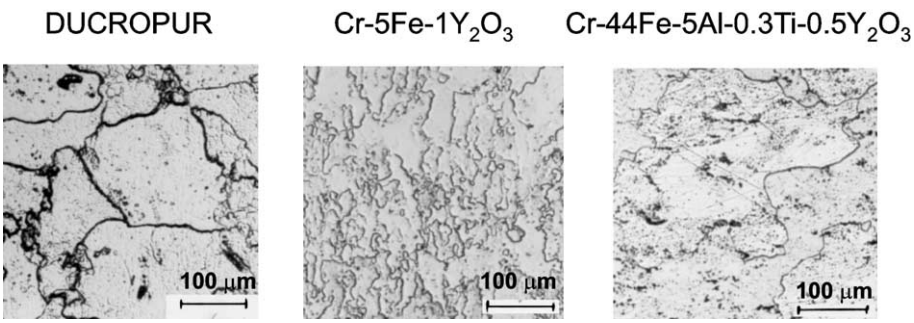

Fig. 1. Optical micrographs of the structure of powder metallurgically processed and sintered Ducropur, Cr–5Fe–$1Y_2O_3$ and Cr–44Fe–5Al–0.3Ti–$0.5Y_2O_3$.

the establishment of such a fine dispersoid structure by mechanical alloying. This problem was overcome by alloying with 5 wt% iron [5].

3. Experimental methods and results

3.1. Mechanical properties

3.1.1. Tensile testing

The tensile properties of the alloys were determined in displacement-controlled tensile tests with strain rates $\dot{\varepsilon}$ in the range of 1×10^{-4} to 1×10^{-3} s^{-1} according to the ASTM standards E8-91 and E21-79(88) [37,38]. Three types of specimen geometries were used. Plane pin-loaded tension test specimens with a cross section of (i) 1 mm × 4 mm and (ii) 3 mm × 3.1 mm shaped by spark erosion and (iii) cylindrical specimens with a diameter of 4 mm on the gauge length produced by machining. A sufficient surface quality of the specimens for tensile testing could only be achieved when new, sharp tools were used for the final machining step. Attempts to improve the surface quality by electropolishing were abandoned because preferential etching of the grain boundaries led to a substantial deterioration of the tensile properties. The central part of the specimens with a constant cross-section area had a length of 20 and 35 mm for the two types of plane pin-loaded specimens, respectively, and 30 mm for the cylindrical specimen type. The cylindrical specimens complied with the shape standard for round machined tension test specimens for powder metallurgical products [37].

The tensile tests were carried out in air, in the temperature range between room temperature (20 °C) and 1000 °C. The specimen temperature was measured with two thermocouples on the upper and lower end of the gauge length and controlled with a three zone resistance furnace. The temperature gradient along a 30 mm gauge was $\leqslant 2$ K. Temperatures above 350 °C could be established and stabilized within 30 min or less. Adjusting the exact temperature and reducing the temperature gradient along the gauge length required more time for lower test temperatures. The overall duration of a tensile test was less than 45 min. After testing the cross section area A at the fracture site of the specimens was determined and normalized to the initial cross section area A_0. Due to the anisotropy of the hot rolled material the cross section became elliptically shaped. Thus, the cross section was calculated as $A = \pi d_1 d_2/4$ where d_1 and d_2 were the major and minor diameters, respectively.

Ducropur, Cr–5Fe–$1Y_2O_3$ and Cr–44Fe–5Al–0.3Ti–$0.5Y_2O_3$ showed pronounced ductility at temperatures above 150, 400 and 500 °C, respectively. Below 300 and 400 °C no valid data could be obtained for the ultimate tensile strength σ_{UTS} of Cr–5Fe–$1Y_2O_3$ and Cr–44Fe–5Al–0.3Ti–$0.5Y_2O_3$, respectively, due to premature brittle failure. Preferential sites for brittle failure were on the radius between the end fillets and the shoulder of the cylindrical specimens where flaws were inevitably introduced by machining. Plane specimens exhibited ductility about 100 °C below the temperature where first ductility of cylindrical specimens was observed. Premature brittle fracture of plane pin-loaded specimens occurred preferentially at the pin holes. Also in these cases flaws on the specimen surfaces resulting from the production process could be identified as crack starters. Only Ducropur exhibited sufficient ductility to obtain valid σ_{UTS} data at room temperature.

Figs. 2–4 present the temperature dependence of the proof stress at 0.2% plastic deformation $\sigma_{0.2}$, of the ultimate tensile strength σ_{UTS} and of the elongation at fracture ε_{frac}. The more brittle alloys Cr–5Fe–$1Y_2O_3$ and Cr–44Fe–5Al–0.3Ti–$0.5Y_2O_3$ exhibit an effect of specimen geometry on the tensile data, which diminishes as temperature increases and the materials gain ductility. The effect is best visible in the proof stress of Cr–5Fe–$1Y_2O_3$ and Cr–44Fe–5Al–0.3Ti–$0.5Y_2O_3$ where the plane pin-loaded specimens exhibit lower $\sigma_{0.2}$ values than the cylindrical specimens. This may be explained by a different constraint and flaws along the edges of plane

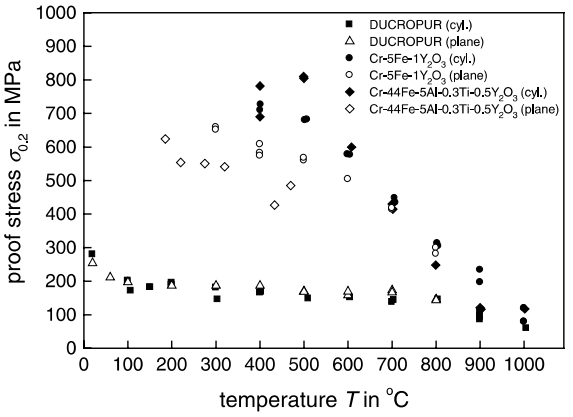

Fig. 2. Temperature dependence of the proof stress $\sigma_{0.2}$ of Ducropur, Cr–5Fe–$1Y_2O_3$ and Cr–44Fe–5Al–0.3Ti–$0.5Y_2O_3$.

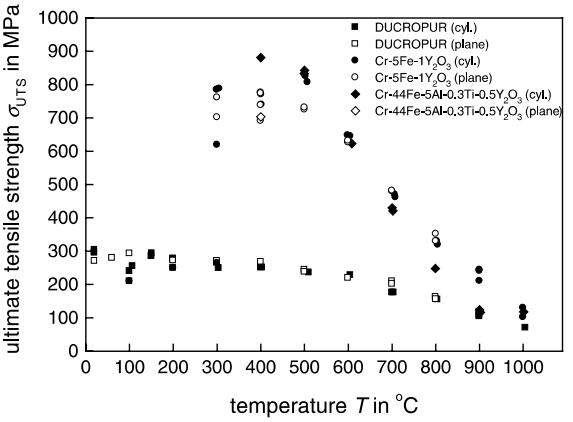

Fig. 3. Temperature dependence of the ultimate tensile strength σ_{UTS} of Ducropur, Cr–5Fe–$1Y_2O_3$ and Cr–44Fe–5Al–0.3Ti–$0.5Y_2O_3$.

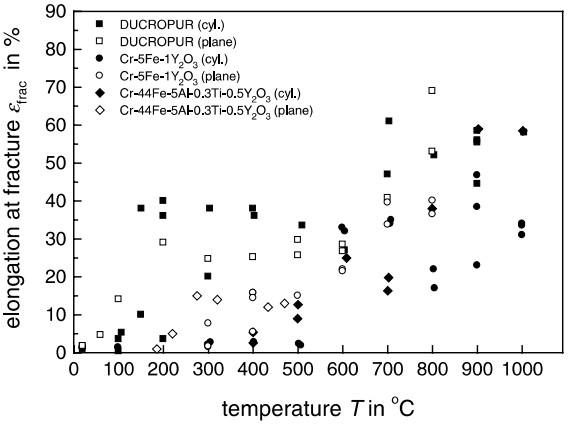

Fig. 4. Temperature dependence of the elongation at fracture ε_{frac} of Ducropur, Cr–5Fe–$1Y_2O_3$ and Cr–44Fe–5Al–0.3Ti–$0.5Y_2O_3$.

pin-loaded specimens caused by the production process. Since plane specimens were produced from sheet material in the final specimen thickness most of their surface was not affected by shaping, whereas the whole surface of cylindrical specimens was newly created by machining. It is supposed that this difference caused a higher density of flaws on cylindrical compared to plane specimens leading to the seemingly higher ductility of plane specimens at lower test temperatures.

In several cases SEM could identify inclusions as failure reason. The powder metallurgical production of the material may result in some microscopic inhomogeneity of the material leading to premature failure at imperfections like inclusions or microscopic voids giving rise to a rather large variation of tensile data.

In the whole investigated temperature range Ducropur exhibits the lowest strength of the three materials as expected for the pure base material. Up to about 600 °C the Cr–44Fe–5Al–0.3Ti–$0.5Y_2O_3$ alloy exceeds the strength of the Cr–5Fe–$1Y_2O_3$ alloy. At higher temperatures Cr–5Fe–$1Y_2O_3$ becomes the strongest of the three materials. However, Cr–5Fe–$1Y_2O_3$ exhibits less ductility in terms of elongation at fracture than Ducropur and Cr–44Fe–5Al–0.3Ti–$0.5Y_2O_3$.

At temperatures above about 600 °C the tensile curves have a characteristic shape reaching their maximum σ_{UTS} at a few % elongation only, followed by a long nearly linear decrease (see Fig. 5). Observation by eye gave no indications for necking at this stage. The onset of substantial necking is related with the accelerated decrease of the engineering stress shortly before failure. Ducropur exhibits pronounced necking, yielding a cross section reduction A/A_0 to 15–20% in the ductile range. At temperatures of at least 500 °C Cr–44Fe–5Al–0.3Ti–$0.5Y_2O_3$ exhibits an intermediate behaviour

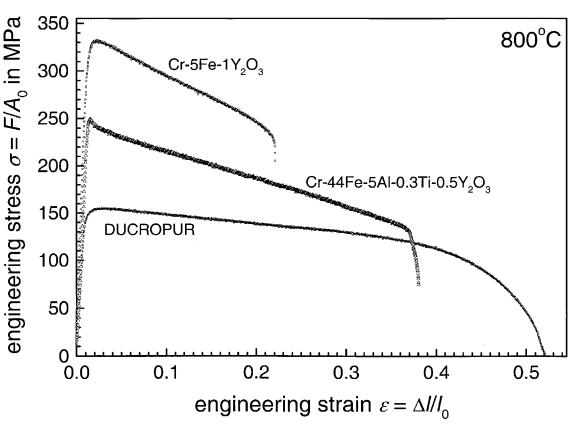

Fig. 5. Comparison of typical tensile curves of the materials Ducropur, Cr–5Fe–$1Y_2O_3$ and Cr–44Fe–5Al–0.3Ti–$0.5Y_2O_3$ tested at 800 °C (strain rate $\dot{\varepsilon} = 3 \times 10^{-4}$ s^{-1}).

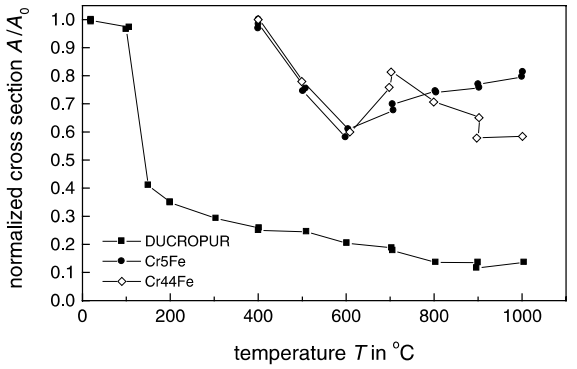

Fig. 6. Cross section A at the fracture site normalized to the initial cross section A_0 for cylindrical specimens of Ducropur, Cr–5Fe–$1Y_2O_3$ and Cr–44Fe–5Al–0.3Ti–$0.5Y_2O_3$ (strain rate $\dot{\varepsilon} = 3 \times 10^{-4}$ s^{-1}).

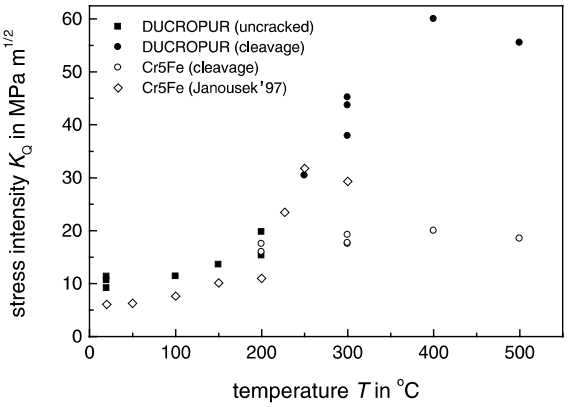

Fig. 7. Fracture toughness K_Q of Ducropur (■, ●) and of Cr–5Fe–$1Y_2O_3$ (○, ◇) as a function of temperature. The filled squares indicate estimates from uncracked specimens, the open and filled circles present results where cleavage rupture initiated in a pre-cracked specimen. The open diamonds refer to data from Janousek [5].

between Ducropur and Cr–5Fe–$1Y_2O_3$ in terms of elongation at fracture, but without showing the pronounced necking of Ducropur. The necking behaviour described by the reduction of the A/A_0 ratio shown in Fig. 6 is similar to that of Cr–5Fe–$1Y_2O_3$ which reaches roughly half of the elongation at fracture of Cr–44Fe–5Al–0.3Ti–$0.5Y_2O_3$ (cf. Fig. 4).

3.1.2. Fracture toughness

Fracture mechanics tests for the determination of fracture toughness in terms of K_{IC} or J_{IC} were performed for Ducropur and Cr–5Fe–$1Y_2O_3$ in air in the temperature range between room temperature and 500 °C with an MTS servohydraulic testing machine (MTS, series 810). Compact test specimens according to ASTM-E399-90 [39] with a thickness of 15 mm (cf. ASTM-E399-90 [39]) were cut by spark erosion from Ducropur and Cr–5Fe–$1Y_2O_3$ plates. Chevron notches were introduced that should facilitate the initiation of a fatigue crack that was propagated by cyclic loading to the required length. At temperatures below 200 °C the brittleness of the materials led to unstable cleavage fracture from the Chevron notch impeding sufficient fatigue crack growth.

The stress intensity factors determined from Ducropur compact test specimens were denoted as K_Q because they were no valid critical stress intensity K_{IC}-values according to the standard ASTM-E399-90 [39]. At temperatures below 200 °C the K_Q values were calculated from the maximum load and the fatigue crack length observed after rupture. These values can be considered as an upper bound of the fracture toughness. The results are plotted in Fig. 7. The circular symbols represent measurements where unstable failure initiated at a fatigue pre-crack that fulfilled the length requirements of the standard. The non-validity with regard to the standard was due to the violation of the size requirements, which limits valid values in Ducropur specimens to 15.5 MPa$\sqrt{\text{m}}$, and partially due to the testing procedure. At higher temperatures J_{IC} tests were performed according to the compliance test method in order to determine the amount of ductile crack growth prior to cleavage failure. The K_Q results evaluated from the initiation of cleavage fracture may be influenced by the pre-deformation of the crack tip region before cleavage fracture intervened. The filled squares in Fig. 7 represent measurements in Ducropur where cleavage fracture occurred before a sufficiently long fatigue crack had grown. These values must be considered as upper bounds for the fracture toughness in this temperature range.

The results for Ducropur show an increase of toughness at about 200 °C thus indicating a brittle-to-ductile transition. However, even at test temperatures of 500 °C fractography revealed cleavage fracture after a small amount of ductile crack growth. Further tests are required to determine the temperature where the material fails completely by ductile tearing without mode conversion to cleavage.

The fracture toughness values obtained in Cr–5Fe–$1Y_2O_3$ with CT specimens are indicated in Fig. 7 by open circles. In addition data from Janousek [5] are included which were obtained from notched four-point bending specimens with 5 mm thickness. Due to specimen size requirements, valid K_{IC} values are limited to about 25 MPa$\sqrt{\text{m}}$. Taking into account that no pre-crack was introduced, these data should be considered as upper bounds, too. Our measurements are in good agreement at 200 °C but indicate rather low K_Q values of

about 15–20 MPa$\sqrt{\text{m}}$ up to 500 °C where still cleavage fracture is observed.

3.1.3. Fractography

SEM was used for fractographic studies of Ducropur tensile specimens and compact specimens. The fracture surfaces were examined with regard to fracture mode and crack initiation sites. In general, the fracture surfaces were oriented perpendicular to the loading direction. Tear ridges separate transgranular cleavage planes with characteristic river patterns (see Fig. 8). Cleavage fracture initiation points, frequently close to the border, were found in most of the specimens and could be associated with discontinuities such as inclusion particles. In Cr–5Fe–1Y_2O_3, again transgranular brittle fracture, characterized by typical cleavage planes, occurred. Fracture initiation points are close to the borders and were associated with stringers. At 400 °C mixed transgranular and intergranular fracture was found.

The fracture surface of a Ducropur compact specimen broken at 400 °C is shown in Fig. 9. The fatigue pre-crack is well distinguishable from a zone in the centre of the specimen with ductile crack growth and from subsequent cleavage zone. Such zones with ductile crack growth prior to cleavage failure were observed at specimens tested at temperatures $\leqslant 250$ °C. At 300 °C, ductile zones with a width of about 2 mm in the centre of the specimen were found. At the lateral specimen surface, where plastic deformation and some necking occur, the zone width was much smaller and sometimes hardly visible.

Cr–5Fe–1Y_2O_3 compact specimens did not exhibit a ductile crack growth zone in the whole temperature range up to 500 °C. Cleavage fracture occurred in all cases without visible plastic deformation at the lateral specimens surfaces.

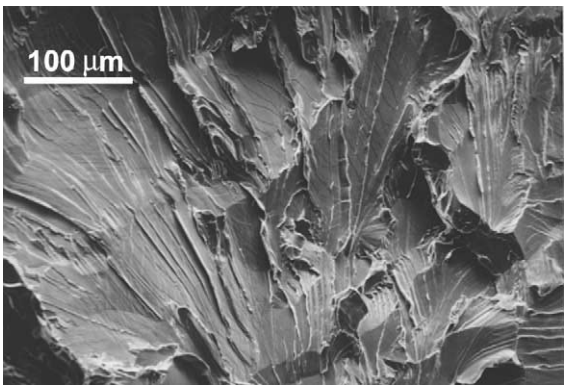

Fig. 8. SEM fractography of a Ducropur compact tension specimen tested at 300 °C. The fracture surface exhibits transgranular cleavage planes with river patterns.

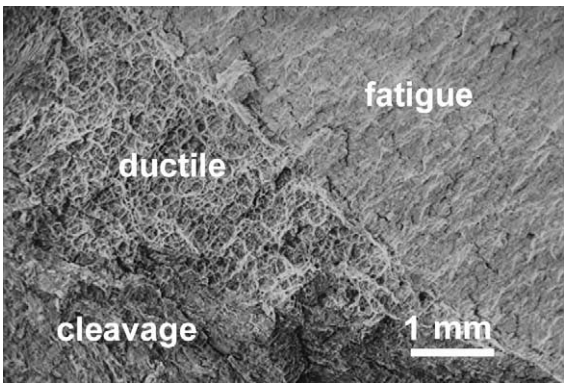

Fig. 9. Rupture surface of a Ducropur compact tension specimen broken at 400 °C. A small zone of ductile crack growth can be distinguished from the fatigue pre-crack and the cleavage rupture.

3.2. Thermal properties

3.2.1. Thermal diffusivity

The thermal diffusivity of the alloys was measured between room temperature and 1000 °C using the laser flash method [40,41]. For this purpose small specimens of 1.5 mm thickness and 10 mm in diameter were heated on one side by a short laser pulse. The temperature increase was detected on the opposite side and the thermal diffusivity was determined from the characteristics of the recorded temperature transient. Several series of tests were performed in vacuum and in argon atmosphere without significantly different results.

The thermal diffusivity of Ducropur, Cr–5Fe–1Y_2O_3 and Cr–44Fe–5Al–0.3Ti–0.5Y_2O_3 is reported in Fig. 10. The unalloyed Ducropur has a significantly higher thermal diffusivity than the other two alloys, however

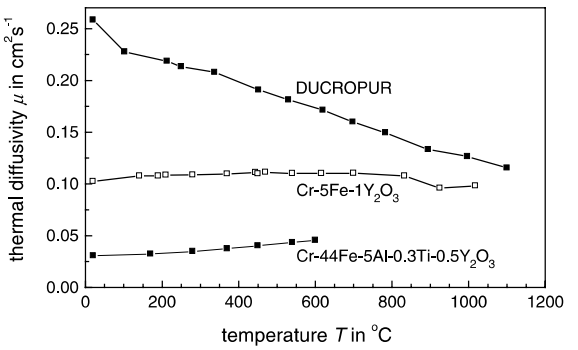

Fig. 10. Temperature dependence of the thermal diffusivity $\mu(T)$ in $\text{cm}^2\,\text{s}^{-1}$ of Ducropur, Cr–5Fe–1Y_2O_3 and Cr–44Fe–5Al–0.3Ti–0.5Y_2O_3 measured between room temperature and 1100, 1000 and 600 °C, respectively.

with a pronounced decrease towards higher temperatures. The iron-rich alloy Cr–44Fe–5Al–0.3Ti–0.5Y_2O_3 exhibits the lowest values. Its low thermal diffusivity together with the most pronounced brittleness encountered in tensile testing and the less favourable low-activation properties of Cr–44Fe–5Al–0.3Ti–0.5Y_2O_3 led its exclusion from the further experimental programme.

3.2.2. Heat capacity at constant pressure

The heat capacity was measured in a differential scanning calorimeter (model DSC 404, manufactured by Netzsch, Germany) using slabs of 1 mm thickness and 6 mm diameter with reference to a sapphire sample of identical dimensions and to an empty platinum crucible. The measurements were carried out in the temperature range between 50 and 1010 °C in argon atmosphere with a heating rate of 20 K/min.

The temperature dependence of the heat capacity of Ducropur and Cr–5Fe–1Y_2O_3 is nearly identical as can be seen from Fig. 11. They show an approximately linear increase between 50 and 1000 °C from 0.48 J/K g to about 0.67 J/K g. Data referring to temperatures lower than 70 °C can be affected by a higher uncertainty due to the relatively small difference between the measurement and the ambient temperature and since the thermal contact between the sample and the crucible improves as temperature increases.

3.2.3. Thermal expansion coefficient

The thermal expansion was measured using cylinders of Ducropur and Cr–5Fe–1Y_2O_3 of 5 mm diameter and 25 mm length with reference to an Al_2O_3 specimen with identical dimensions in a differential dilatometer (model 402ED manufactured by Netzsch, Germany). The dilatometer measured the expansion difference between the samples and the alumina cylinder. The thermal expansion data of the alumina reference are compiled in the standard DIN 51045/89. Since the positions of the thermocouple used to control the furnace and the specimen were not identical a slight difference between the measured temperature and the real temperature along the specimen was expected. When heating up the furnace at a certain rate this could result in a delay reaching the indicated temperature along the specimen. The correspondence of the temperature measured by the built-in thermocouple with the real temperature of the specimen was checked by comparing the signals of the built-in thermocouple, a second thermocouple at the specimen site and the lecture of the incorporated mechanical micrometer. As a consequence of these tests the temperature increase for the measurements was fixed to a rate of 1 K/min in order to minimize the temperature error.

The temperature dependence of the average thermal expansion coefficient $\alpha_m = \Delta L/(L\,\Delta T)$ is presented in Fig. 12. Here, ΔT denotes the temperature difference $T - T_0$ with $T_0 = 20$ °C and $\Delta L = L(T) - L_0$ the length difference being $L_0 = L(T_0)$ the specimen length at 20 °C. Typical values for Ducropur and Cr–5Fe–1Y_2O_3 range between 8×10^{-6} and 11×10^{-6} K^{-1} which are remarkably low values compared to other materials under consideration as structural materials for fusion applications (cf. Table 2).

3.3. Calculated thermal and thermomechanical properties

3.3.1. Thermal conductivity

With the results for the temperature dependence of the thermal expansion coefficient $\alpha(T)$, the heat capacity

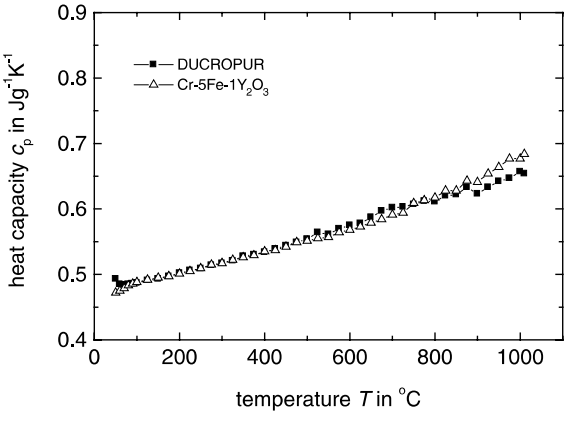

Fig. 11. Temperature dependence of the heat capacity at constant pressure $c_p(T)$ in $J\,g^{-1}\,K^{-1}$ of Ducropur and Cr–5Fe–1Y_2O_3 between room temperature and 1000 °C.

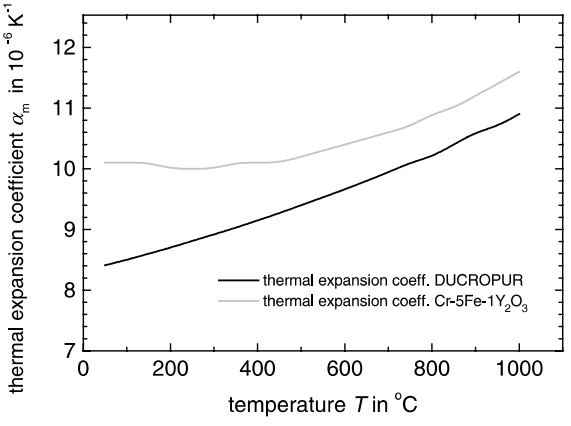

Fig. 12. Temperature dependence of the average thermal expansion coefficient $\alpha(T)$ in 10^{-6} K^{-1} of Ducropur and Cr–5Fe–1Y_2O_3 in the temperature range between room temperature and 1000 °C.

Table 2
Overview on key properties of Ducropur, Cr–5Fe–1Y_2O_3, the vanadium-based alloys V–15Cr–5Ti and V–4Cr–4Ti, the reduced activation ferritic steels F82H and the martensitic and austenitic stainless steels MANET and AISI 316 L

Property		Ducropur	Cr–5Fe–1Y_2O_3	V–4Cr–4Ti	V–15Cr–5Ti	F82H	MANET	AISI 316 L
T_m (°C)	–	1863 [3]	1805–1825 [3]	1875–1925 [45]	1890 [52]	1450–1500 [3,59]	1450–1530 [59]	1375–1425 [60,61]
ϱ (M g m^{-3})	RT	7.200 [42,44]	7.190 [5]	6.050 [45]	6.100 [52]	7.890 [53]	7.757 [58]	7.963 [58,59]
E (GPa)	RT	280 [42]	280 ± 20 [7]	125.6 [46,47]	126 [52]	217 [54,55]	217 [58]	192–195 [61,62]
v	RT	0.22 [42]	0.22 [5]	0.367 [46,47]	0.36 [52]	0.29 [54,55]	0.27 [58]	0.28 [61]
α (K^{-1})	RT	8.4×10^{-6}	10.0×10^{-6}	9.1×10^{-6} [48]	9.3×10^{-6} [52]	10.4×10^{-6} [53,54]	10.0×10^{-6} [58,63]	16.2×10^{-6} [58]
	400 °C	9.1×10^{-6}	10.1×10^{-6}	9.71×10^{-6}	10.2×10^{-6}	11.5×10^{-6}	11.9×10^{-6}	16.2×10^{-6}
	600 °C	9.70×10^{-6}	10.4×10^{-6}	10.0×10^{-6}	10.5×10^{-6}	12.1×10^{-6}	12.4×10^{-6}	18.3×10^{-6}
	800 °C	10.1×10^{-6}	10.9×10^{-6}	10.2×10^{-6}	10.9×10^{-6}	–	–	19.0×10^{-6}
λ (W m^{-1} K^{-1})	RT	90.0	34.6	30.4 [48]	21.0 [52]	34.5 [53–55]	24.1 [58,63]	14.7 [58]
	400 °C	76.0	41.8	33.9	26.8	31.6	25.9	20.0
	600 °C	70.0	44.2	35.2	29.5	32.8	26.4	22.9
	800 °C	63.2	47.0	37.1	32.5	–	–	25.7
σ_y (MPa)	RT	260	918 [5]	335–378 [49–51]	590 [52]	550 [53,56,57]	614 [58,63]	207–270 [58,62]
	400 °C	165	730	216	350	485	519	151–168
	600 °C	162	560	230	340	295	313	128–138
	800 °C	140	340	235 [51,50]	290	–	–	118
DBTT (°C)		150–500	400–500	−200 ··· −150 [28]	−150 ··· −50 [52]	−50 [80]	−30 ··· +20 [82]	–
		100–400 [7]		−155 [78]		−75 [81]	−15 [58]	
K_{IC} (MPa$\sqrt{m}$)		⩽10 (RT) ≈55 (DBBT)	6.4 (RT) [5] 15–20 (DBBT) [5]	250 (RT) [77] 100 (DBBT) [79]	–	150 (RT) [79] 100 (−100 °C) [79]	–	–

T_m denotes the melting temperature, ϱ the mass density, E the Young's modulus and v the Poisson coefficient, α stands for the average thermal expansion coefficient, λ for the thermal conductivity. σ_y denotes the yield stress.

$c_p(T)$ and the thermal diffusivity $\mu(T)$, the thermal conductivity can be calculated according to

$$\lambda(T) = \varrho(T)c_p(T)\mu(T) = \frac{\varrho_0}{1+3\alpha(T)T}c_p(T)\mu(T). \quad (4)$$

Fig. 13 presents the results for Ducropur and Cr–5Fe–1Y_2O_3, for which all measurements ($\alpha(T)$, $c_p(T)$, $\mu(T)$) were performed. Ducropur shows a higher thermal conductivity than Cr–5Fe–1Y_2O_3 but with a pronounced decrease from about 90 W m^{-1} K^{-1} at room temperature to about 57 W m^{-1} K^{-1} at 1000 °C. The thermal conductivity of Cr–5Fe–1Y_2O_3 shows a slight increase in the same temperature range from about 35 W m^{-1} K^{-1} to about 47 W m^{-1} K^{-1} at 1000 °C.

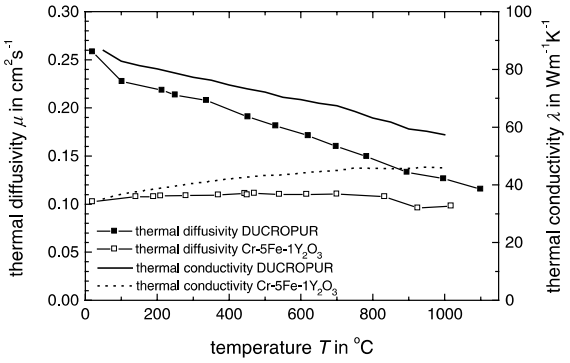

Fig. 13. Temperature dependence of the thermal conductivity $\lambda(T)$ in W m^{-1} K^{-1} calculated according to Eq. (4) from the thermal diffusivity $\mu(T)$ in Fig. 10 and the data reported in Figs. 11 and 12 for Ducropur and Cr–5Fe–1Y_2O_3 up to 1000 °C.

3.3.2. Thermal stress factor

The thermal stress factor as defined in Eq. (3) can be derived after measuring the thermal expansion coefficient α and calculating the thermal conductivity λ from experimental data. For the calculations presented in Fig. 14 the proof stress values at 0.2% plastic deformation has been used instead of σ_y. The temperature

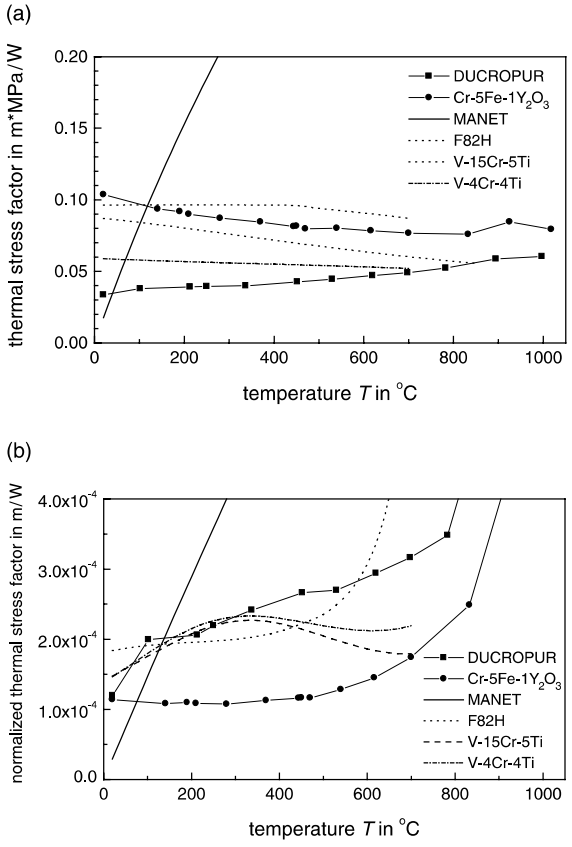

Fig. 14. Temperature dependence of (a) the thermal stress factor Θ and (b) the thermal stress factor Θ^* normalized to $\sigma_{0.2}$ (defined in Eq. (3)) of Ducropur, Cr–5Fe–1Y_2O_3, the vanadium alloys V–4Cr–4Ti, V–15Cr–5Ti and the ferritic/martensitic steels F82H and MANET.

dependence of Young's modulus has been linearly extrapolated from the data reported by Simmons and Wang [42] in the temperature range between 77 and 500 K. These data are based on well documented X-ray and ultrasound measurements by Summer and Smith [43] and Bolef and Klerk [44]. These data agree with the data given by Plansee [7] but are significantly higher than Young's modulus reported in the Metals Handbook [45]. The Poisson ratio was approximately considered as constant with $\nu = 0.22$ [42].

The very low figure for Ducropur in Fig. 14(a) compared to other low-activation materials (about 0.34 MPa m/W at 20 °C) results from its favourable combination of high-thermal conductivity and low-thermal expansion coefficient. After normalizing the thermal stress factor to the yield stress in Fig. 14(b), Cr–5Fe–1Y_2O_3 takes over the leading position due to its high strength at elevated temperatures.

The numerical data required to calculate the thermal stress factor for the competitors as first wall and blanket materials V–4Cr–4Ti [46–51], V–15Cr–5Ti [52], the ferritic reduced activation steel F82H [53–57] and the ferritic steel MANET [58,59] are compiled in Table 2. The table contains data for the austenitic stainless steel AISI 316 L for comparison [58–62].

4. Discussion

4.1. Thermal properties and thermal stresses

Table 2 compares key properties of Ducropur and Cr–5Fe–1Y_2O_3 with those of other candidate materials for structural applications in fusion technology. The lower thermal conductivity of Cr–5Fe–1Y_2O_3 compared to pure chromium in Fig. 13 can be understood by the solid solution of iron atoms in the chromium matrix which reduces the lattice symmetry and increases the number of scatter centres for phonons and electrons, thus reducing the thermal conductivity. In the same way defects introduced in the bulk material by radiation will degrade the thermal conductivity because they present deviations from the perfect crystalline state acting as scatter centres for phonons. The effects of grain size and of dispersed Y_2O_3 particles on the thermal conductivity of the materials are expected to be insignificant. The solid solution of Fe in Cr changes also the interatomic potential whose anharmonic part gives rise to the thermal expansion. Thus, the alloying effect on the thermal expansion coefficient observed in Fig. 12 is plausible.

The high-thermal conductivity combined with the low-thermal expansion coefficient of Ducropur and Cr–5Fe–1Y_2O_3 results in a low-thermal stress factor. Hence, in this respect, these materials may easily compete with vanadium-based alloys. The high-yield strength of Cr–5Fe–1Y_2O_3 at temperatures up to 1000 °C yields the absolute lowest value of the thermal stress factor normalized to the yield strength of all metallic materials discussed for first wall and blanket applications. In spite of the rather low-yield strength Ducropur can compete with the vanadium-based alloys.

The effect of the figures on a first wall design can be illustrated making use of Eq. (2). Assuming a heat flux of 0.5 MW/m^2 and a service temperature of 300 °C, the maximum thickness d_{max} of a first wall or blanket material that can withstand the thermomechanical load is determined by the thickness which makes the thermal stress equal to the yield stress of the material. Taking the data from Fig. 14b (Θ^* (300 °C)), values for d_{max} of 1.4 mm for stainless steel AISI 316 L, 4.7 mm for MANET, 9 mm for Ducropur and the vanadium alloys but 20 mm for Cr–5Fe–1Y_2O_3 are obtained.

A lot of work has been done on ceramic SiC_f/SiC_m fibre-matrix composites [30–32,64–66]. Various fibre concepts have been investigated and different types of composites are under investigation using different fibres

Table 3
Compilation of the DBTT of Ducropur, Cr–5Fe–1Y_2O_3 and Cr–44Fe–5Al–0.3Ti–0.5Y_2O_3 derived from different experiments

Experimental source	Ducropur °C	Cr–5Fe–1Y_2O_3 °C	Cr–44Fe–5Al–0.3Ti–0.5Y_2O_3 °C
Elongation at fracture	≈150	≈400	400–500
Cross section reduction	100–150	400–500	400–500
Fracture toughness	≈250	>500	–
Fractography	≈500	>500	–

Tensile test data refer to cylindrical specimens with 4 mm in diameter.

and production techniques. The physical and mechanical properties of fibres, SiC bulk material and of the resulting composites exhibit appreciable scatter. Therefore it is difficult to get conclusive data which allow a direct comparison of the thermal stress factor with the metallic materials presented in Fig. 14. The performance of a ceramic fibre-matrix composite depends strongly on the fabrication process of the fibres and the composite. The composite exhibits a pronounced anisotropy of its physical and mechanical properties. Based on the best data compiled in [64] ($\lambda = 323\ \mathrm{W\,m^{-1}K^{-1}}$, $\alpha = 0.5 \times 10^{-6}\ \mathrm{K^{-1}}$, $E = 107$ GPa, $\nu = 0.2$, $\sigma_y = 130$ MPa) the values calculated for the thermal stress factors Θ and Θ^* are $2 \times 10^{-4}\ \mathrm{m\,MPa\,W^{-1}}$ and $1.6 \times 10^{-6}\ \mathrm{m\,W^{-1}}$, respectively. These values are a factor of about 100 better than those of the best metallic material, i.e., the chromium alloy. This potential may however only be reached with perfect composites. Due to the severe degradation of the thermal conductivity by neutron irradiation, initial thermal conductivities are requested of $\geqslant 300\ \mathrm{W\,m^{-1}\,K^{-1}}$ and $\geqslant 150\ \mathrm{W\,m^{-1}\,K^{-1}}$ at room temperature and 1000 °C, respectively [64]. Further problems concern the mismatch of the elastic moduli and of the thermal expansion coefficients between SiC fibres and the SiC matrix. Thermomechanical loading may thus lead to problems along the fibre-matrix interface [66] and to matrix cracking. Since the thermal conductivity of the SiC fibres (≈5–15 $\mathrm{W\,m^{-1}\,K^{-1}}$), is much lower than that of the SiC matrix (≈400 $\mathrm{W\,m^{-1}\,K^{-1}}$ (single crystal SiC)) the heat flows entirely through the matrix and matrix cracking will appreciably reduce the thermal conductivity. Using data given by Riccardi et al. [31] ($\lambda = 13\ \mathrm{W\,m^{-1}\,K^{-1}}$, $\alpha = 2.5 \times 10^{-6}\ \mathrm{K^{-1}}$, $E = 200$ GPa, ($\nu = 0.2$), $\sigma_{UTS} = 300$ MPa) the values calculated for the thermal stress factors Θ and Θ^* are $4.8 \times 10^{-2}\ \mathrm{m\,MPa\,W^{-1}}$ and [1] $2 \times 10^{-4}\ \mathrm{m\,W^{-1}}$, which is again in the range of the best metallic materials.

4.2. Ductile-to-brittle transition temperature

Table 3 compiles the DBTT values derived from different tests and specimen geometries. Cylindrical Ducropur specimens exhibit significant elongation at fracture and cross section reductions already at test temperatures around 150 °C. From fracture toughness testing one would conclude a DBTT of at least 250 °C, and the fractography cleavage fracture was observed at even higher temperatures. Such a discrepancy has already been discussed by Thornley and Wronski [67] for chromium and tungsten. These authors defined transition temperatures for ductility, T_T, and failure mode, T_F, based on the definition of brittle materials by Bridgman [68] and Cottrell [69] on one side and of Orowan [70] on the other side. Bridgman and Cottrell define materials as brittle if they fail after only microscopic plastic deformation [68,69]. Hence the transition temperature T_T is defined as the temperature where macroscopic plastic deformation can be observed in tensile testing. Orowan, on the other hand, considered brittle fracture as the process of catastrophic crack propagation to failure under the action of a tensile stress [70]. Therefore, T_F defines the fracture mode transition temperature which is derived from fractography. Thornley and Wronski found a grain size dependence of the transition temperatures with $T_T = (255 \pm 5)$ K and $T_F = (525 \pm 40)$ K for coarse grained chromium with a mean grain size of 225 μm and $T_T = (660 \pm 4)$ K and $T_F = (660 \pm 4)$ K for the fine grained chromium with 34 μm grain size [67]. The tendency that the difference between T_T and T_F vanishes with decreasing grain size was also found in tungsten [67].

In view of the grain size of our alloys, our value of about 500 °C for Ducropur (grain size 82 μm) agrees rather well with the finding of Thornley and Wronski for T_F [67]. However, a comparison of their data with the results compiled in Table 3 has to consider the microstructure differences between the well recrystallized specimens used by Thornley and Wronski and our powder metallurgically processed material and the oxide particle strengthening of the alloys. In the case of Cr–5Fe–1Y_2O_3 fracture toughness and subsequent fractography studies were performed up to 500 °C, which is not sufficient to reveal a possible difference between T_T and T_F in this alloy.

In iron-based alloys with chromium contents in the range between 0.5 and 42 wt%, the room temperature values of σ_y and σ_{UTS} increase approximately linearly

[1] As a value for σ_y was not found in Ref. [31], σ_{UTS} was used for the calculation of Θ^*.

with the chromium content, and the elongation at fracture decreases inversely [8,71,72]. This trend depends also on factors like microstructure and the level of impurities. The toughness is reported to decrease with increasing chromium content but brittle behaviour can be avoided even at chromium contents of 35 wt%, provided that the level of carbon and nitrogen impurities can be kept below 0.02 wt% [8,73]. However, the tolerable content of impurities becomes smaller with increasing chromium content. Therefore, extrapolating this tendency from the iron-rich part of the chromium–iron system to high-chromium alloys, it can be expected that the potential pickup of interstitial solute atoms especially at high-temperatures might become an issue for chromium alloys. It can be expected that chromium behaves like other body-centred cubic (bcc) materials, tungsten, molybdenum, tantalum, niobium and iron which show a pronounced temperature and strain-rate dependence of the flow stress at temperatures sufficiently low to hinder the free motion of screw dislocations [74]. Interstitial atoms like nitrogen, oxygen and carbon hinder the thermally activated formation of kink-pairs and the subsequent motion of the kinks along the screw dislocations [74]. In this way the mobility of screw dislocations is appreciably reduced and hence the ductility of bcc materials [74–76].

The observation of an apparently lower DBTT for plane tensile test specimens than for cylindrical test specimens may find a geometrical explanation in the different constraint and different shaping procedures affecting the density of flaws (machining of cylindrical specimens vs. spark erosion of plane specimens).

In order to allow a rough comparison of the performance of Ducropur and Cr–5Fe–1Y_2O_3 with vanadium alloys and steels, typical room temperature data of the fracture toughness [77–80] and DBTT data [28,52,58,78,81,82] are compiled in Table 2. Low-fracture toughness values and the propensity to brittle fracture up to 500 °C may limit the utility of Cr–5Fe–1Y_2O_3. Ducropur has a significantly lower strength but displays higher ductility. Fracture toughness values are significantly higher than those in Cr–5Fe–1Y_2O_3 and indicate a DBTT around 250 °C (cf. Table 3). Although the low-thermal stress levels under a given heat flux load may compensate for the low-temperature brittleness, chromium and chromium alloys will show their full advantage at operation temperatures above the 300 °C of the water cooled ITER design. The lack of low-temperature ductility is a concern for materials processing, start-up and shutdown procedures. Problems of shaping may be overcome by powder metallurgical processing and hot isostatic pressing. However, ductility may be improved using high-purity grades of chromium with even better low-activation characteristics.

4.3. Microstructure refinement

Hardness and yield strength σ_y of a material usually increase with decreasing grain size d. This behaviour can be described by the Hall–Petch relation [83,84],

$$\sigma_y = a - bd^{-1/2}, \tag{5}$$

and is microscopically determined by dislocation gliding within the grains; a and b are material specific constants. Below a certain grain size this relation breaks down. The material gains ductility and loses strength due to atomic rearrangement events in the grain boundaries with only a minor part being caused by dislocation gliding inside the grains. Hence, the softening observed in nanocrystalline materials is caused by a larger fraction of atoms in less densely packed grain boundary areas [85]. This reverse Hall–Petch effect is expected at a grain size below 10–20 nm and even in the absence of microporosity [85]. In contrary to super plasticity the reverse Hall–Petch effect is not based on thermally activated dislocation glide processes and is not accompanied by a pronounced temperature and strain-rate dependence of the flow stress [85].

One possibility to refine the microstructure of the currently available materials is to reduce the particle size of the powders used for the initial mechanical alloying step. It could be shown that the grain size of pure chromium powder and the ingredients iron and yttria for the Cr–5Fe–1Y_2O_3 alloy could be decreased to about 25 nm after 50 h of high-energy ball milling under a vacuum of 10^{-6} bar [86], leading to microstrains of the order 5×10^{-3} in the particles [86]. However, an investigation of the uptake of interstitial impurities during ball milling and the stability of grain size during and after compactation at different temperatures needs further investigation.

Severe plastic deformation by equal channeling [87] or severe plastic torsional straining [87,88] is another method to nanostructure materials by introducing high-angle (sub-)grain boundaries. Results of a first attempt to introduce an ultra-fine grained structure in Ducropur and Cr–5Fe–1Y_2O_3 by severe torsional straining were reported in Ref. [89] and indicate that this method may be a starting point for improving the low-temperature mechanical properties of Ducropur and Cr–5Fe–1Y_2O_3.

Billets of Ducropur and Cr–5Fe–1Y_2O_3 were subjected to an isostatic pressure of up to 6 GPa placing them between a fixed lower anvil and a rotating upper anvil [88]. Up to five complete turns of the anvil were performed. Processing temperatures between 400 and 600 °C were required due to limited room temperature ductility. Transmission electron microscopy, selected area diffraction patterns and X-ray texture measurements revealed an ultra-fine grained structure with high-angle grain boundaries after such processing. The

dislocation density in these grain boundaries was determined to be up to 1×10^{15} m^{-2} whereas it was about three orders of magnitude lower in the cell interior. At a deformation temperature of 540 °C, a mean grain size of 0.3 and 0.5 μm was obtained in Ducropur and Cr–5Fe–1Y_2O_3, respectively, which was equivalent to a grain refinement by a factor of about 260 and 22, respectively. The different degree of obtainable refinement may be due to the different initial grain size, but also an effect of the Y_2O_3 particles is likely. An analysis in terms of the Hall–Petch relation shows that the increase of σ_y is lower than expected from a reduction in grain size. However, the grain size in the range of a few hundred nanometers is still too large to observe the reverse Hall–Petch relation [85]. In the case of Ducropur the microstructure refinement was accompanied by an increase of the Vickers microhardness from 1.75 GPa to above 6 GPa and to about 3 GPa for processing at room temperature and at 540 °C, respectively. The ultra-fine microstructure was stable against annealing for 30 min up to 450 °C. Annealing at 900 °C re-established the hardness value before processing.

Tensile tests were performed on Ducropur after microstructure refinement in the temperature range between 20 and 350 °C. At e.g. 300 °C, an ultimate tensile strength of 480 MPa was obtained, which is twice as high as in the coarse grained material. Fig. 15 displays stress displacement curves of bending tests carried out at 100 °C. They indicate that severe plastic deformation at 540 °C yields an appreciable strengthening of the material without an apparent loss of ductility. Taking the difference between the ultimate tensile strength σ_{UTS} and the rupture stress σ_r in Fig. 2 as indicator for ductility, a considerable improvement was achieved from 107 MPa to up to 476 MPa for coarse (initial) and fine-grained (processed) material, respectively. Similar values were

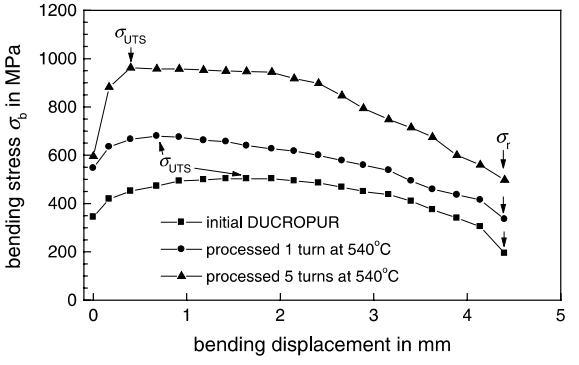

Fig. 15. Bending stress σ_b vs bending displacement, measured at 100 °C, for as received Ducropur and after processing by torsion deformation at 540 °C for 1 and 5 turns [89]. The values used as ultimate strength σ_{UTS} and rupture strength σ_r in Section 4.3 are indicated.

obtained for bending at 200 °C whereas at room temperature no effect was visible.

A dislocation dynamic model of the ductile-to-brittle transition by Hähner and Stamm [90] may give an explanation for the observed effect that an increase of tensile strength by reducing the effective grain size must not necessarily be accompanied by increasing the brittleness of the material. The question whether an existing crack can exhibit stable crack propagation is related to the competition of three factors: (i) the emission of dislocations from the crack tip, (ii) crack shielding due to the plastic zone and (iii) cleavage [90]. In the present case it appears reasonable to assume that stable crack propagation is favoured by the reduction of the slip length of dislocations due to the increase of the dislocation density by severe plastic deformation [90].

Severe plastic deformation may be helpful to overcome problems with brittle chromium and chromium alloys during fabrication of components at room temperature, provided technologically significant batches of the material could be processed. However, the thermal stability of the microstructure limits the usefulness of such processing. Therefore it appears more promising to further exploit the potential of high-energy ball milling for microstructure refinement and to investigate possible measures to avoid or reduce contamination.

4.4. Behaviour under irradiation

Irradiation effects on high-purity chromium and Cr–5Fe–1Y_2O_3 have not yet been investigated. However, literature on irradiated iron-based chromium alloys [8,91,92] and chromium-based iron alloys [93] gives some indication.

In high-chromium Fe–Cr alloys toughness is strongly affected by σ phase formation and phase decomposition into α and α′. These phase changes become more pronounced with increasing chromium content, although corrosion properties, high-temperature strength and magnetic properties become more attractive.

Investigations on Fe–Cr alloys with chromium contents between 9 and 50 wt% by Wakai et al. [91] after electron irradiation indicate embrittlement due to the formation of dislocation loops decorated by α′-phase. Neutron irradiation experiments on Fe–(9–30)Cr alloys at 673 K to a dose of 0.3 dpa revealed larger increases of the yield strength in alloys with higher chromium content [92]. Although α′-phase is formed more easily in alloys with higher chromium content, the growth of the loops is slower in these cases [8]. Irradiation hardening increases with increasing chromium and impurity contents [92]. In the chromium-rich part of the phase diagram a single-phase system is expected [3]. Therefore, the irradiation-induced formation of brittle σ-phase [93] should effectively be reduced in the case of Cr–5Fe–1Y_2O_3 with only 5 wt% iron, and an improved radiation

resistance may be expected compared to already examined iron–chromium alloys. Furthermore, high-chromium alloys are expected to exhibit superior swelling resistance to ferritic steels [8].

Chakin et al. [93] studied the formation of the brittle σ phase in Cr–Fe alloys under neutron irradiation on the chromium-rich side of the Cr–Fe system. Three alloys were tested after irradiation with neutrons in the temperature range between 600 and 750 °C. The irradiation of the Cr–0.32La–0.26Ta–0.40 V alloy at 650 °C with a neutron flux of 2.8×10^{26} m^{-2} ($E > 0.1$ MeV) resulted in the formation of uniformly distributed voids with a mean diameter of 6 nm and a density of 2×10^{16} cm^{-3}. The DBTT was shifted up to 600 °C. In an alloy with the composition Cr–10Fe–0.2Zr–0.2Y irradiated at 600 °C with a neutron flux of 4.7×10^{26} m^{-2}, non-uniformly distributed voids with a mean diameter of 10 nm, a density of 4×10^{15} cm^{-3} and precipitates with a diameter of 40–50 nm were found. The DBTT remained as low as 200 °C. After neutron irradiation of Cr–35Fe–0.2Zr–0.2Y no voids were observed but precipitates which approach a size of 1 μm. By microdiffraction methods the precipitates could be identified as σ phase [93]. The experiments of Chakin et al. [93] indicate that an optimum iron content might exist where σ phase can be produced during neutron irradiation, but with tolerable effect on brittleness.

4.5. Compatibility with hydrogen

As the planned service temperature of a fusion reactor rises, problems of brittleness may become less important and high-temperature strength, corrosion resistance, chemical compatibility with coolants as well as pickup of hydrogen and other interstitial impurities will prevail. In this case, chromium alloys may gain an advantage over vanadium alloys due to the lower solubility for hydrogen and their good high-temperature corrosion properties. Although the equilibrium hydrogen concentration in vanadium is considered very low [16] the solubility of hydrogen in chromium at 500 °C is orders of magnitude lower than in vanadium (see Refs. [94,95] and citations there) which reduces the tritium inventory especially when used as blanket material. In chromium no effect of hydrogen on the ductile-to-brittle behaviour has been found because hydrogen picked up at high-temperatures leaves the material nearly completely during cooling [95]. For vanadium alloys Röhrig et al. reported that hydrogen concentrations of up to 2.5 at.% can be tolerated before leading to catastrophic failure [96], however, the impact of this concentration on the tritium inventory has not been discussed. Moreover, pre-exposure to oxygen lowers the tolerable hydrogen concentrations appreciably [96]. In V–4Cr–4Ti the interaction of hydrogen with the irradiated alloy has already been studied [97]. However, the hydrogen permeation of vanadium and chromium alloys cannot yet be compared because reliable hydrogen diffusion data in chromium are lacking [98].

Acknowledgements

The authors thank Dr M. Janousek, Dr D. Rickerby, Dr F. Dos Santos Marques, Dr F. Lakestani, Dr V. Provenzano, Prof. R. Valiev and Dr G. Valdré for fruitful discussions. The authors are indebted with S. Colpo, H. Kolbe, A. Volcan, A. Pisoni and F. Cernuschi for technical support during the various measurements.

Appendix A. Fit functions for thermal and mechanical properties

For the following polynomial fit functions temperature data have to be taken in °C.

A.1. Ducropur

- Proof stress at 0.2% plastic deformation (between 20 and 1000 °C)

$$\sigma_{0.2} = (254.04 - 0.56483T + 0.00118T^2 - 8.24413 \times 10^{-7}T^3)\ \text{MPa}. \quad (A.1)$$

Correlation factor $R = 0.88554$.

- Ultimate tensile strength (between 20 and 1000 °C)

$$\sigma_{\text{UTS}} = (277.37 - 0.01618T - 3.78777 \times 10^{-5}T^2 - 1.62003 \times 10^{-7}T^3)\ \text{MPa}. \quad (A.2)$$

Correlation factor $R = 0.96151$.

- Thermal diffusivity (between 20 and 1000 °C)

$$\mu(T) = (0.2542 - 1.73475 \times 10^{-4}T + 8.015 \times 10^{-8}T^2 - 3.5161 \times 10^{-11}T^3)\ \text{cm}^2\,\text{s}^{-1}. \quad (A.3)$$

Correlation factor $R = 0.99025$.

- Thermal expansion coefficient (between 20 and 1000 °C)

$$\alpha(T) = (8.3159 + 1.80901 \times 10^{-3}T + 6.45421 \times 10^{-7}T^2 + 1.27483 \times 10^{-10}T^3) \times 10^{-6}\ \text{K}^{-1}. \quad (A.4)$$

Correlation factor $R = 0.99963$.

- Specific heat at constant pressure (between 20 and 1000 °C)

$$c_p(T) = (0.48047 + 6.34753 \times 10^{-5}T + 2.34120 \times 10^{-7}T^2 - 1.27824 \times 10^{-10}T^3)\ \text{J}\,\text{g}^{-1}\,\text{K}^{-1}. \quad (A.5)$$

Correlation factor $R = 0.99635$.

- Thermal conductivity (between 20 and 1000 °C)

$$\lambda(T) = (87.56671 - 0.04179T + 3.15147 \times 10^{-5}T^2 - 2.06676 \times 10^{-8}T^3)10^{-6}\ \mathrm{W\,K^{-1}\,m^{-1}}. \quad (A.6)$$

Correlation factor $R = 0.99639$.

A.2. Cr–5Fe–1 Y_2O_3

- Proof stress at 0.2% plastic deformation (between 300 and 1000 °C)

$$\sigma_{0.2} = (214.59 + 3.22434T - 0.0059T^2 + 2.5564 \times 10^{-6}T^3)\ \mathrm{MPa}. \quad (A.7)$$

Correlation factor $R = 0.99482$.

- Ultimate tensile strength (between 400 and 1000 °C)

$$\sigma_{\mathrm{UTS}} = (1086.47 - 0.44433T - 5.5168 \times 10^{-4}T^2)\ \mathrm{MPa}. \quad (A.8)$$

Correlation factor $R = 0.96151$.

- Thermal diffusivity (between 20 and 1000 °C)

$$\mu(T) = (0.10255 + 3.12057 \times 10^{-5}T - 2.13821 \times 10^{-8}T^2 - 1.51848 \times 10^{-11}T^3)\ \mathrm{cm^2\,s^{-1}}. \quad (A.9)$$

Correlation factor $R = 0.84779$.

- Thermal expansion coefficient (between 20 and 1000 °C)

$$\alpha(T) = (10.183 - 1.31538 \times 10^{-3}T + 2.72499 \times 10^{-6}T^2)10^{-6}\ \mathrm{K^{-1}}. \quad (A.10)$$

Correlation factor $R = 0.99701$.

- Specific heat at constant pressure (between 20 and 1000 °C)

$$c_p(T) = (0.46683 + 1.93264 \times 10^{-4}T - 1.22719 \times 10^{-7}T^2 + 1.43947 \times 10^{-10}T^3)\ \mathrm{J\,g^{-1}\,K^{-1}}. \quad (A.11)$$

Correlation factor $R = 0.99842$.

- Thermal conductivity (between 20 and 1000 °C)

$$\lambda(T) = (34.10722 + 0.02624T - 1.72921 \times 10^{-5}T^2 + 2.97932 \times 10^{-9}T^3)10^{-6}\ \mathrm{W\,K^{-1}\,m^{-1}}. \quad (A.12)$$

Correlation factor $R = 0.99698$.

A.3. Cr–44Fe–5Al–0.3Ti–0.5 Y_2O_3

- Proof stress at 0.2% plastic deformation (between 400 and 1000 °C)

$$\sigma_{0.2} = (1585.00 - 1.87037T + 3.23597 \times 10^{-4}T^2)\ \mathrm{MPa}. \quad (A.13)$$

Correlation factor $R = 0.95143$.

- Ultimate tensile strength (between 400 and 1000 °C)

$$\sigma_{\mathrm{UTS}} = (1908.37 - 2.66773T + 8.06986 \times 10^{-4}T^2)\ \mathrm{MPa}. \quad (A.14)$$

Correlation factor $R = 0.96910$.

- Thermal diffusivity (between 20 and 700 °C)

$$\mu(T) = (0.03059 - 4.26563 \times 10^{-7}T + 6.84103 \times 10^{-8}T^2 - 4.36207 \times 10^{-11}T^3)\ \mathrm{cm^2\,s^{-1}}. \quad (A.15)$$

Correlation factor $R = 0.99992$.

References

[1] W.D. Klopp, J. Met. 23 (1969) 23.
[2] W.D. Klopp, J. Less-Common Met. 42 (1975) 261.
[3] B. Massalski, in: Binary Alloy Phase Diagrams, 2nd Ed., ASM, Metals Park, OH, 1991, p. 822.
[4] R. Eck, H.-P. Martinz, T. Sakaki, M. Kato, Mater. Sci. Eng. A 120 (1989) 307.
[5] M. Janousek, Fortschritt-Berichte, VDI-Reihe 5, Nr. 476, VDI, Düsseldorf, 1997.
[6] W. Köck, H.-P. Martinz, H. Greiner, M. Janousek, Proceedings of the 4th International Symposium on Solid Oxide Fuel Cells, Yokohama, Japan, 1995;
M. Dokiya, O. Yamamoto, H. Tagawa, S.C. Singhal (Eds.), Proceedings of the Electrochemistry Society, vol. 95-1, Pennington, NJ, 1995, p. 841.
[7] Metallwerke Plansee AG, Austria, product information Chromium Based Alloys for Solid Oxide Fuel Cell (SOFC) Components.
[8] A. Hishinuma, S. Isozaki, S. Takaki, K. Abiko, Phys. Stat. Sol. (a) 160 (1997) 431.
[9] M. Zucchetti, M. Merola, J. Nucl. Mater. 233–237 (1996) 1486.
[10] P. Rocco, M. Zucchetti, Fusion Eng. Des. 15 (1992) 235.
[11] P. Rocco, M. Zucchetti, J. Nucl. Mater. 212–215 (1994) 649.
[12] H. Stamm, M.R. Bonansinga, F. Dos Santos Marques, P. Hähner, H. Kolbe, A. Volcan, J. Nucl. Mater. 258–263 (1998) 1756.
[13] Standardization of Radioactive Waste Categories, IAEA, Technical Reports Series no. 101, 1970.
[14] E.V. Dyomina, P. Fenici, V.P. Kolotov, M. Zucchetti, J. Nucl. Mater. 258–263 (1998) 1784.
[15] E.E. Bloom, J. Nucl. Mater. 258–263 (1998) 7.
[16] D.L. Smith, M.C. Billone, S. Majumander, R.F. Mattes, D.-K. Sze, J. Nucl. Mater. 258–263 (1998) 65.
[17] B. van der Schaaf, Fusion Eng. Des. 51–52 (2000) 43.
[18] B. van der Schaaf, D.S. Gelles, S. Jitsukawa, A. Kimura, R.L. Klueh, A. Möslang, G.R. Odette, J. Nucl. Mater. 283–287 (2000) 52.
[19] K. Ehrlich, E.E. Bloom, T. Kondo, J. Nucl. Mater. 283–287 (2000) 79.

[20] ITER Documentation Series, no. 3, ITER Concept Design, IEA, Vienna, 1989.
[21] G. Shatalov, I. Kirillov, U. Sokolov, Yu. Strebkov, N. Vasiliev, RF DEMO Team, Fusion Eng. Des. 51–52 (2000) 289.
[22] S.J. Zinkle, N.M. Ghoniem, Fusion Eng. Des. 51–52 (2000) 55.
[23] A. Hishinuma, A. Kohyama, R.L. Klueh, D.S. Gelles, W. Dietz, K. Ehrlich, J. Nucl. Mater. 258–263 (1998) 193.
[24] A. Kohyama, A. Hishinuma, D.S. Gelles, R.L. Klueh, W. Dietz, K. Ehrlich, J. Nucl. Mater. 233–237 (1996) 138.
[25] M. Tamura, H. Hayakawa, M. Tanimura, A. Hishinuma, T. Kondo, J. Nucl. Mater. 141–143 (1986) 1067.
[26] R.W. Conn, E.E. Bloom, J.W. Davis, R.E. Gold, R. Little, K.R. Schultz, D.L. Smith, F.W. Wiffen, UCLA Report PPG-728, UCLA, 1983.
[27] R.J. Kurtz, K. Abe, V.M. Chernov, V.A. Kazakov, G.E. Lucas, H. Matsui, T. Muroga, G.R. Odette, D.L. Smith, S.J. Zinkle, J. Nucl. Mater. 283–287 (2000) 70.
[28] S.J. Zinkle, H. Matsui, D.L. Smith, A.F. Rowcliffe, E. van Osch, K. Abe, V.A. Kazakov, J. Nucl. Mater. 258–263 (1998) 205.
[29] S.N. Votinov, M.I. Solonin, Yu.I. Kazennov, V.P. Kondratjev, A.D. Nikulin, V.N. Tebus, E.O. Adamov, S.E. Bougaenko, Yu.S. Strebkov, A.V. Sidorenkov, V.B. Ivanov, V.A. Kazakov, V.A. Evitikhin, I.E. Lyublinski, V.M. Trojanov, A.E. Rusanov, V.M. Chernov, G.A. Birgevoj, J. Nucl. Mater. 233–237 (1996) 370.
[30] A. Hasegawa, A. Kohyama, R.H. Jones, L.L. Snead, B. Riccardi, P. Fenici, J. Nucl. Mater. 283–287 (2000) 128.
[31] B. Riccardi, P. Fenici, A. Frias Rebelo, L. Giancarli, G. Le Marois, E. Philippe, Fusion Eng. Des. 51–52 (2000) 11.
[32] P. Fenici, A.J. Frias Rebelo, R.H. Jones, A. Kohyama, L.L. Snead, J. Nucl. Mater. 258–263 (1998) 215.
[33] F.A. Garner, J.M. McArthy, in: An Assessment of Fe–Cr–Mn Austenitic Alloys for Fusion Service Using Fast Reactor Activation, ASTM STP 1047, ASTM, Philadelphia, PA, 1990, p. 19.
[34] G.R. Romanoski, L.L. Snead, R.L. Klueh, D.T. Hoelzer, J. Nucl. Mater. 283–287 (2000) 642.
[35] A.H. Sully, E.A. Brandes (Eds.), Chromium, second ed., Butterworth, London, 1967.
[36] Annual Book of ASTM Standards Vol. 03.01, Standard Test Methods for Determining Average Grain Size, E 112-88, ASTM, Philadelphia, PA, 1992.
[37] Annual Book of ASTM Standards Vol. 03.01, Standard Test Methods of Tension Testing of Metallic Materials, E 8-91, ASTM, Philadelphia, PA, 1992.
[38] Annual Book of ASTM Standards Vol. 03.01, Standard Practice for Elevated Temperature Tension Tests of Metallic Materials, E 21-79, ASTM, Philadelphia, PA, 1992 (reapproved 1988).
[39] Annual Book of ASTM Standards Vol. 03.01, Standard Test Method for Plane-Strain Fracture Toughness of Metallic Materials, E 399-90, ASTM, Philadelphia, PA, 1992.
[40] J. Parker, R.J. Jenkins, C.P. Butler, G.L. Abbot, J. Appl. Phys. 32 (1961) 1679.
[41] British Standard No. BS 7134, Part 4, Section 4.2, Testing of engineering ceramics. Thermo-physical properties. Method for the determination of thermal diffusivity by the laser flash (or heat pulse) method, British Standards Institution, London, 1990.
[42] G. Simmons, H. Wang, Single Crystal Elastic Constants and Calculated Aggregate Properties: MIT, Cambridge, MA (USA) and London (UK), 1971.
[43] A. Summer, J.F. Smith, J. Appl. Phys. 34 (1963) 2691.
[44] D.I. Bolef, J. De Klerk, Phys. Rev. 129 (1963) 1063.
[45] Metals Handbook, 9th Ed., vol. 2, Properties and Selection: Nonferrous Alloys and Pure Metals, ASM, Metals Park, OH, 1979, p. 822 (V), p. 724 (Cr).
[46] R.J. Farraro, R.B. McLellan, Met. Trans. 10A (1979) 1699.
[47] W.A. Simpson, in: Fusion Materials—Semiannual Progress Report, DOE/ER-0313/16, Oak Ridge National Laboratory, 1994, p. 258.
[48] W.D. Porter, R.B. Dinwiddie, M.L. Grossbeck, in: Fusion Materials—Semiannual Progress Report for Period Ending March 31, 1994, DOE/ER-0313/16, Oak Ridge National Laboratory, 1994, p. 260.
[49] M.C. Billone, H.M. Chung, D.L. Smith, J. Nucl. Mater. 258–263 (1998) 1523.
[50] A.F. Rowcliffe, D.T. Hoelzer, S.J. Zinkle, in: Fusion Materials—Semiannual Progress Report, DOE/ER-0313/26, Oak Ridge National Laboratory, 1999, p. 25.
[51] A.F. Rowcliffe, S.J. Zinkle, D.T. Hoelzer, J. Nucl. Mater. 283–287 (2000) 508.
[52] D.L. Smith, B.A. Loomis, D.R. Diercks, J. Nucl. Mater. 135 (1985) 125.
[53] N. Yamanouchi, M. Tamura, H. Hayakawa, A. Hishinuma, T. Kondo, J. Nucl. Mater. 191–194 (1992) 822.
[54] K. Shiba, N. Yamanouchi, A. Kohyama, in: Fusion Materials—Semiannual Progress Report, DOE/ER-0313/20, Oak Ridge National Laboratory, 1996, p. 190.
[55] K. Shiba, A. Hishinuma, A. Tohyama, K. Masamura, Japan Atomic Energy Research Institute Report JAERI-Tech 97-038, 1997.
[56] J.P. Robertson, R.L. Klueh, K. Shiba, A.F. Rowcliffe, in: Fusion Materials—Semiannual Progress Report, DOE/ER-0313/23, 1997, p. 179.
[57] K. Shiba, M. Suzuki, A. Hishinuma, J. Nucl. Mater. 233–237 (1996) 309.
[58] M. Küchle, Material Data Base for the NET Test Blanket Design Studies, European Test Blanket Development Program, Test Blanket Advisory Group, Kernforschungszentrum Karlsruhe, 1990, unpublished.
[59] C.W. Wegst (Ed.), Stahlschlüssel, Verlag Stahlschlüssel Wegst, Marbach, Germany, 1989.
[60] Metals Handbook, 9th ed., Vol. 3—Properties and Selection: Stainless Steels, Tool Materials and Special-Purpose Metals, American Society for Metals, Metals Park, OH, 1980.
[61] A.E. Walter, A.B. Reynolds, Fast Breeder Reactors, Pergamon, New York, 1981.
[62] Cases of ASME Boiler and Pressure Vessel Code, Code Case N-47-17, 1980.
[63] E. Zolti, Comparative Review and Interim Data Base of Candidate Structural Materials, Elementary Tailored Martensitic Steel, SEAFP/R-M4/1, 1992.
[64] V. Barabash, M. Akiba, J.P. Bonal, G. Federici, R. Matera, K. Nakamura, H.D. Pacher, M. Rödig, G. Vieider, C.H. Wu, J. Nucl. Mater. 258–263 (1998) 149.
[65] K. Fujii, R. Yamada, J. Nucl. Mater. 258–263 (1998) 1953.

[66] M. Saito, A. Hasegawa, S. Ohtuska, K. Abe, J. Nucl. Mater. 258–263 (1998) 1562.
[67] J.C. Thornley, A.S. Wronski, Met. Sci. J. 6 (1972) 113.
[68] P.W. Bridgman, J. Appl. Phys. 18 (1947) 246.
[69] A.H. Cottrell, Trans. Met. Soc. AIME 212 (1958) 192.
[70] E. Orowan, Rep. Prog. Phys. 12 (1948) 185.
[71] S. Nakazawa, Y. Sato, T. Ozaki, in: Characteristics of High Purity Fe–Cr Alloys, Japan Iron and Steel Corporation, 1995, p. 2.
[72] K. Kondo, Y. Okada, in: Characteristics of High Purity Fe–Cr Alloys, Japan Iron and Steel Corporation, 1995, p. 20.
[73] W.O. Binder, H.R. Spedelow Jr., Trans. ASME 43 (1951) 759.
[74] B. Šestàk, A. Seeger, Z. Metallkd. 69 (1978) 195, 355, 425.
[75] M. Werner, Phys. Stat. Sol. (a) 104 (1988) 63.
[76] L. Hollang, M. Hommel, A. Seeger, Phys. Stat. Sol. (a) 160 (1997) 329.
[77] G.R. Odette, G.E. Lucas, E. Donahue, J.W. Sheckherd, J. Nucl. Mater. 233–237 (1996) 502.
[78] E. Donahue, G.R. Odette, G.E. Lucas, in: Fusion Materials—Semiannual Progress Report, DOE/ER-0313/26, Oak Ridge National Laboratory, 1999, p. 33.
[79] A.F. Rowcliffe, J.P. Robertson, R.L. Klueh, K. Shiba, D.J. Alexander, M.L. Grossbeck, S. Jitsukawa, J. Nucl. Mater. 258–263 (1998) 1275.
[80] H.-X. Li, R.H. Jones, J.P. Hirth, D.S. Gelles, J. Nucl. Mater. 233–237 (1996) 258.
[81] R.L. Klueh, K. Ehrlich, F. Abe, J. Nucl. Mater. 191–194 (1992) 116.
[82] M. Rieth, B. Dafferner, J. Nucl. Mater. 233–237 (1996) 229.
[83] E.O. Hall, Proc. Phys. Soc. Lond. B 64 (1951) 747.
[84] N.J. Petch, J. Iron Steel Inst. 174 (1953) 25.
[85] J. Schiotz, F.D. Di Tolla, K.W. Jacobson, Nature 391 (1998) 561.
[86] G. Valdrè, private communication.
[87] R.Z. Valiev, Mater. Sci. Engng. 234–236 (1997) 59.
[88] I.V. Alexandrov, Y.T. Zhu, T.C. Lowe, R.K. Ismagaliev, R.Z. Valiev, Nanostructured Mater. 10 (1998) 45.
[89] H. Stamm, U. Holzwarth, F. Lakestani, R. Valiev, V. Provenzano, A. Volcan, J. Nucl. Mater. 283–287 (2000) 597.
[90] P. Hähner, H. Stamm, Acta Met. Mater. 43 (1995) 2797.
[91] E. Wakai, A. Hishinuma, Y. Kato, H. Yano, S. Takaki, K. Abiko, J. Physique Coll. C7, suppl. J. Phys. (Paris) III 5 (1995) C7-277.
[92] E. Wakai, A. Hishinuma, T. Sawai, S. Kato, S. Isozaki, S. Takaki, K. Abiko, Phys. Stat. Sol. (a) 160 (1997) 441.
[93] V. Chakin, V. Kazakov, Yu. Goncharenko, Z. Ostrovsky, J. Nucl. Mater. 233–237 (1996) 573.
[94] G. Hörz, E. Fromm, in: E. Fromm, E. Gebhardt (Eds.), Gase und Kohlenstoff in Metallen, Reine und angewandte Metallkunde in Einzeldarstellungen, Band 26, Springer, Berlin, 1976, p. 441.
[95] H. Jehn, in: E. Fromm, E. Gebhardt (Eds.), Gase und Kohlenstoff in Metallen, Reine und angewandte Metallkunde in Einzeldarstellungen, Band 26, Springer, Berlin, 1976, p. 521.
[96] H.D. Röhrig, J.R. DiStefano, L.D. Chitwood, J. Nucl. Mater. 258–263 (1998) 1356.
[97] A.Kh. Klepikov, O.G. Romanenko, Y.V. Chikhray, I.L. Tazhibaeva, V.P. Shestakov, G.R. Longhurst, Fusion Eng. Des. 51–52 (2000) 127.
[98] Landolt-Börnstein, Numerical Data and Functional Relationships in Science and Technology, New Series, Group III: Crystal and Solid State Physics, in: H. Mehrer (Ed.), Diffusion in Solid Metals and Alloys, vol. 26, Springer, Berlin, 1990.